Bulk Power System Dynamics and Control - VII, August 19-24, 2007, Charleston, South Carolina, USA

Dynamics of a Microgrid Supplied by Solid Oxide Fuel Cells[1]

Eric M. Fleming Ian A. Hiskens
Department of Electrical and Computer Engineering
University of Wisconsin - Madison
Madison, WI 53706 USA

***Abstract*— The paper presents a model for a solid oxide fuel cell (SOFC) stack operating at relatively low pressures. The model incorporates the electrochemical reaction dynamics and the major voltage losses in SOFCs, but is not concerned with the thermal dynamics. A DC-DC boost converter interfaces the SOFC stack to a DC bus, where an ultra-capacitor provides energy storage. The paper presents a control system for the converter which regulates the DC-bus voltage along with the fuel cell current. A control strategy is proposed for the inverter that interfaces the SOFC plant to the AC grid. The controller regulates the grid-side voltage and the active power delivered to the grid, and takes into account the phase-locked loop (PLL) dynamics. The results of an example in which two SOFC plants provide power to a microgrid are presented. The simulation includes disconnection from the main grid, autonomous operation, and re-synchronization with the main grid.**

Keywords: Solid oxide fuel cells, microgrid dynamics, inverter control.

I. Introduction

Distributed generation sources are becoming more prevalent within distribution systems, with a growing role in applications ranging from combined heat and power to reliability enhancement. This trend has motivated the concept of a microgrid, which generically consists of multiple generators and loads, interconnected by a subsection of the distribution system [1], [2]. Microgrids, by definition, should be able to operate when grid-connected, or islanded (autonomous), and should transition reliably through the connection/disconnection process.

In parallel with the trend towards greater distributed generation, fuel cell technology has been advancing rapidly, as a result of significant research and development efforts. It is therefore likely that fuel cells will make an increasingly important contribution to distributed generation. In particular, solid oxide fuel cells (SOFCs) are well suited to stationary applications where there is a requirement for combined heat and power.

Microgrids that are supplied solely by inverter-based sources, such as fuel cells, may have no rotating inertia. As a result, the frequency of the AC voltages and currents must be established by the inverter controls. Generally this is achieved through the use of a phase-locked loop (PLL) which establishes a reference signal for power electronic firing. The dynamic behavior of the PLLs therefore has an important influence on the microgrid frequency. Furthermore, with no rotating inertia present, interactions between inverter controls may be potentially destabilizing.

[1]Research supported by the National Science Foundation through grant ECS-0524744, "System Integration of Distributed Generation".

The paper investigates the dynamic behavior of microgrids that are supplied by SOFCs. Initially, a dynamic model of an SOFC stack is developed. The grid connection of an SOFC is then considered, with particular emphasis on controller design for the DC-DC converter and the DC-AC inverter. A microgrid example is used to explore the behavior of an SOFC-supplied microgrid.

II. SOFC Stack Model

A. Background

The operation of all fuel cells is based on the reaction of hydrogen with oxygen to produce water:

$$2H_2 + O_2 \rightarrow H_2O.$$

In order to extract current, and thus electric power, from a fuel cell, the above reaction must be separated into two half-reactions. In an SOFC, these half-reactions take the form [3], [4],

$$H_2 + O^{2-} \rightarrow H_2O + 2e^-$$
$$O_2 + 4e^- \rightarrow 2O_{2-}.$$

The first of these half-reactions takes place at the anode, and the second takes place at the cathode. The electrons released in the anode half-reaction flow through an external circuit as current and return to the cathode to react with oxygen molecules. The oxygen ions released at the cathode flow through an electrolyte to the anode, where they react with hydrogen [4]–[7]. Since one fuel cell produces only about 1 volt across its terminals, in practice many cells are stacked in series to produce a useable voltage [7].

This paper presents a model for an SOFC stack which incorporates the electrochemical reaction dynamics and the major voltage losses. The thermal dynamics are not included, as the associated time constants are much longer than those of the electrochemical response [4], [6]. The fuel supplied to the SOFC plant is natural gas, which must undergo reforming in order to extract the hydrogen used in the fuel cell reaction. The model presented in this paper assumes that reforming is done in an external fuel processor and pure hydrogen is supplied to the anode channel. It is also necessary to supply oxygen to the cathode reaction. The model assumes that this is achieved via an air compressor which is providing a constant flow rate of air into the cathode channel.

The electrochemical reaction of a fuel cell is spatially distributed, occurring over the membrane that separates the anode and cathode. Therefore, the composition of the gas inside each electrode channel varies along the channel length.

For instance, in the anode, the partial pressure of hydrogen is highest at the inlet orifice and decreases across the length of the channel as it is consumed, and is therefore lowest at the outlet orifice. This idea is used in the SOFC model presented in [4]. It is common, however, for this distributed reaction to be modeled using states that capture average behavior. In particular, average partial pressures are used for the gases within the anode and cathode in all model calculations. The SOFC models presented in [3], [6] use this idea, as does the model presented in this paper.

B. Electrode models

An important aspect of the electrode models is the determination of the flow rates of gases out of each channel. The outlet flow rate is dependent on the area as well as other properties of the orifice through which the gas flows, which can be represented by a valve constant. If the orifice is fixed, the outlet flow rate is coupled with the flow rate of gas into the respective channel as well as the pressure inside the channel. In particular, specifying one of these quantities (inlet flow rate or pressure) dictates the other. The model in this paper uses a specified inlet flow rate and a fixed outlet orifice to determine the channel pressures. This is consistent with SOFC models presented in [3], [6]. The SOFC model in [4] uses a different approach in which the inlet flow rate and the total pressure inside each channel are both specified. This requires the use of a pressure regulator, which acts like an adjustable valve at the outlet orifice and therefore eliminates the need for an orifice equation.

If the pressure difference across an orifice is relatively small, the flow through the orifice is considered unchoked, and the volumetric or mass flow rate is proportional to the square root of the pressure difference [8]–[10]. However, if the pressure difference is large, the flow is considered choked, and the volumetric or mass flow rate through the orifice can be approximated as being proportional to the upstream pressure. The boundary between these two types of flow is defined by the critical ratio of upstream to downstream pressure, which is equal to 1.894 [8]. The SOFC models in [3], [6] assume the pressure inside the channels is high enough that the outlet flow can be considered choked, and they make the simplification of defining the outlet flow rate of each species as being proportional to its partial pressure inside the channel. The model described in this paper assumes that the stack is operated at a sufficiently low pressure that the outlet flow is unchoked and therefore uses the square root relationship in calculating the outlet flow.

C. Anode model

The gases inside the anode are hydrogen and water vapor. With p_{H_2} and p_{H_2O} as the partial pressures of hydrogen and water vapor, respectively, in the anode, the average molar mass of the anode gas can be found as follows:

$$M_a = \frac{p_{H_2} M_{H_2} + p_{H_2O} M_{H_2O}}{p_{H_2} + p_{H_2O}}, \tag{1}$$

where M_{H_2} and M_{H_2O} are the molar masses of hydrogen and water vapor, respectively. Assuming the gases obey the ideal gas law,

$$pV = nRT, \tag{2}$$

the density of the anode gas can then be found as

$$\rho_a = \frac{m_a}{V_a} = \frac{nM_a}{V_a} = \frac{pM_a}{RT} = \frac{(p_{H_2} + p_{H_2O})\, M_a}{RT}, \tag{3}$$

where m_a is the mass of gas inside the anode channel, V_a is the volume of the anode channel, R is the gas constant ($8.31 \frac{J}{mol \cdot K}$), and T is the operating temperature. Assuming unchoked flow, the volumetric flow rate of gas out of the anode [8]–[10] is given by,

$$Q_a = C_{fa} A_a \sqrt{\frac{2}{\rho_a} (p_{H_2} + p_{H_2O} - p_{atm})} \tag{4}$$

where C_{fa} is the anode flow coefficient, A_a is the anode valve area, p_{atm} is the atmospheric pressure, and Q_a has units of (m^3/s).

Again assuming the ideal gas law holds, the molar outlet flow rates of the two component gases can be determined as,

$$N^o_{H_2} = \frac{Q_a p_{H_2}}{RT} \tag{5}$$

$$N^o_{H_2O} = \frac{Q_a p_{H_2O}}{RT} \tag{6}$$

where these quantities have units of (mol/s). The molar outlet flow rates are used in the differential equations governing changes in hydrogen and water vapor partial pressures, which also are based on the ideal gas law [3], [4], [6],

$$\frac{d}{dt} p_{H_2} = \frac{RT}{V_a} \left[N^{in}_{H_2} - N^o_{H_2} - \frac{N_o I}{2F} \right] \tag{7}$$

$$\frac{d}{dt} p_{H_2O} = \frac{RT}{V_a} \left[\frac{N_o I}{2F} - N^o_{H_2O} \right] \tag{8}$$

where $N^{in}_{H_2}$ is the hydrogen molar inlet flow rate, N_o is the number of cells in the stack, I is the stack current, and F is Faraday's constant ($96485 \frac{Coulombs}{mol}$). The term $\frac{N_o I}{2F}$ in the first differential equation is the molar rate of hydrogen used up in the reaction, and likewise the corresponding term in the second differential equation is the molar rate of water vapor produced.

D. Cathode model

A similar formulation can be used to determine the molar outlet flow rates of oxygen and nitrogen from the cathode. The input air is assumed to have a nitrogen-to-oxygen molecular ratio of 78 to 21, and the effects of smaller components of air such as carbon dioxide are ignored. The model equations are as follows:

Average molar mass:

$$M_c = \frac{p_{N_2} M_{N_2} + p_{O_2} M_{O_2}}{p_{N_2} + p_{O_2}} \tag{9}$$

Gas density:

$$\rho_c = \frac{M_c (p_{N_2} + p_{O_2})}{RT} \tag{10}$$

Volumetric outlet flow rate:

$$Q_c = C_{fc} A_c \sqrt{\frac{2}{\rho_c}\left(p_{N_2} + p_{O_2} - p_{atm}\right)} \tag{11}$$

Oxygen molar outlet flow rate:

$$N_{O_2}^o = \frac{Q_c p_{O_2}}{RT} \tag{12}$$

Nitrogen molar outlet flow rate:

$$N_{N_2}^0 = \frac{Q_c p_{N_2}}{RT} \tag{13}$$

Partial pressure variations:

$$\frac{d}{dt} p_{O_2} = \frac{RT}{V_c}\left[N_{O_2}^{in} - \frac{N_o I}{4F} - N_{O_2}^o\right] \tag{14}$$

$$\frac{d}{dt} p_{N_2} = \frac{RT}{V_c}\left[\frac{78}{21} N_{O_2}^{in} - N_{N_2}^o\right] \tag{15}$$

Note that the molar rate of oxygen reacted has a 4 in the denominator rather than a 2. This is because half as many moles of oxygen are used in the reaction as moles of hydrogen. Also note that there is no term in the differential equation for nitrogen partial pressure corresponding to a reaction rate since nitrogen doesn't participate in the reaction.

E. Electrical model

The reversible, or open circuit, potential of an SOFC is given by the Nernst equation [7],

$$E = \frac{N_o}{2F}\left[-\Delta g_f^o + RT \ln\left(\frac{p_{H_2} \cdot p_{O_2}^{1/2}}{p_{H_2O} \cdot p_{atm}^{1/2}}\right)\right] \tag{16}$$

where Δg_f^o is the change in the molar specific Gibbs free energy of formation for the fuel cell reaction, which depends on the operating temperature. For the typical operating temperature range of SOFCs (above 800^oC), the relationship can be approximated by [7],

$$-\Delta g_f^o = 188600 - 56\left(T - 1073.15\right). \tag{17}$$

There are three main types of losses in a fuel cell, contributing to three different voltage drops which subtract from the open circuit potential. These are known as the activation, ohmic, and concentration losses.

The activation loss is caused by the kinetics of the chemical reactions taking place at the fuel cell electrodes, which limit how fast the reactants can be consumed [7]. The resulting voltage drop is modeled in a piecewise fashion,

$$\eta_{act} = \begin{cases} \frac{RT}{4F}\frac{j}{j_o} & j \le j_o \\ \frac{RT}{2F}\ln\left(\frac{j}{j_o}\right) + \frac{RT}{4F}\frac{j}{j_o} & j > j_o \end{cases} \tag{18}$$

where j is the current density, which is equal to the stack current divided by the fuel cell area, $j = I/A$. Equation (18) is an approximation of the Butler-Volmer equation [5]. At low currents, the relationship between activation drop and current is approximately linear. Above j_o, known as the exchange current density, the relationship is logarithmic.

The ohmic loss is caused by resistance to electron flow through the electrode materials as well as resistance to ion flow through the electrolyte [6]. The voltage drop is modeled with a resistance, r, whose value depends on the operating temperature of the fuel cell,

$$r = 0.2 \cdot \exp\left[-2870\left(\frac{1}{1196.15} - \frac{1}{T}\right)\right]. \tag{19}$$

The concentration loss is due to the limited rate at which reactant concentrations can change, which limits the rate at which the reactants can be transported to the electrode surfaces [7]. This voltage drop is modeled as [5], [6],

$$\eta_{con} = -\frac{RT}{4F}\ln\left(1 - \frac{j}{j_l}\right) \tag{20}$$

where j_l is known as the limiting current density.

Finally, the terminal voltage of the fuel cell stack is given by [5]–[7],

$$V_{fc} = E - \eta_{act} - rI - \eta_{con}. \tag{21}$$

F. Modes of operation

There are two basic modes in which fuel cells are operated, constant input and constant utilization. In constant input mode, the inlet flow rates of hydrogen to the anode, $N_{H_2}^{in}$, and oxygen to the cathode, $N_{O_2}^{in}$, are set to fixed values. In constant utilization mode, the inlet flow rate of hydrogen is controlled so that the ratio of hydrogen consumed in the reaction to hydrogen supplied to the anode is regulated to a set value. This ratio is known as the fuel utilization and is defined by [4],

$$U_{H_2} = \frac{\frac{N_0 I}{2F}}{N_{H_2}^{in}}. \tag{22}$$

The control for constant utilization can be implemented using current feedback to adjust the hydrogen input flow rate [4]. The fuel processor can be modeled as a first-order delay transfer function [4], [11]. A block diagram of the model implementation of constant utilization is shown in Figure 1. The corresponding equations are,

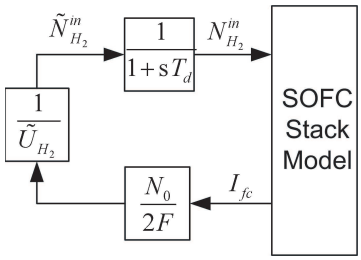

Fig. 1. Constant utilization implementation.

$$\tilde{N}_{H_2}^{in} = \frac{N_o I}{2F\tilde{U}_{H_2}} \tag{23}$$

$$\frac{d}{dt}\left(N_{H_2}^{in}\right) = \frac{1}{T_d}\left(\tilde{N}_{H_2}^{in} - N_{H_2}^{in}\right). \tag{24}$$

The steady-state plot of current versus voltage for a fuel cell stack is known as the polarization curve. Figure 2 shows polarization curves for the two basic modes of operation. The constant input case uses the parameters in Table I. The constant utilization case uses the same parameters, except that

TABLE I

SOFC MODEL PARAMETERS.

parameter	value	units
T	1273.15	K
V_a	0.2	m^3
V_c	0.2	m^3
$N^{in}_{H_2}$	2.0	$\frac{mol}{s}$
$N^{in}_{O_2}$	1.0	$\frac{mol}{s}$
N_o	384	-
A	0.1	m^2
A_a	.0025	m^2
A_c	.0025	m^2
C_{fa}	.75	-
C_{fc}	.75	-
p_{atm}	101325	Pa
M_{H_2}	2.016×10^{-3}	$\frac{kg}{mol}$
M_{H_2O}	18.016×10^{-3}	$\frac{kg}{mol}$
M_{N_2}	28.014×10^{-3}	$\frac{kg}{mol}$
M_{O_2}	31.998×10^{-3}	$\frac{kg}{mol}$
j_o	1500	$\frac{A}{m^2}$
j_l	10000	$\frac{A}{m^2}$
T_d	1	s

the constant hydrogen input flow is replaced by a hydrogen utilization of 0.8.

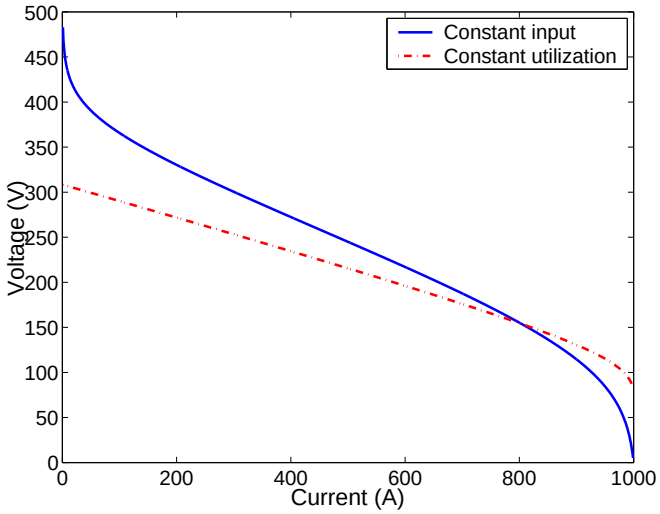

Fig. 2. SOFC polarization curves.

The curve for constant input mode has three identifiable regions [5]. At low currents, the curve is steep. This is known as the activation region, since the activation loss is the main factor contributing to voltage drop. As the current increases, the curve becomes less steep and is nearly linear for a broad range of currents. This is known as the ohmic region, since the predominant voltage drop is ohmic. At high currents, the curve becomes steep again due to the predominance of the concentration voltage drop, and hence this portion of the curve is called the concentration region.

The constant utilization polarization curve does not have the steepness at low currents like that for constant input. The constant utilization curve sits below the constant input curve for currents where the utilization in the constant input case is less than that of the constant utilization case, and sits above the constant input curve at higher currents.

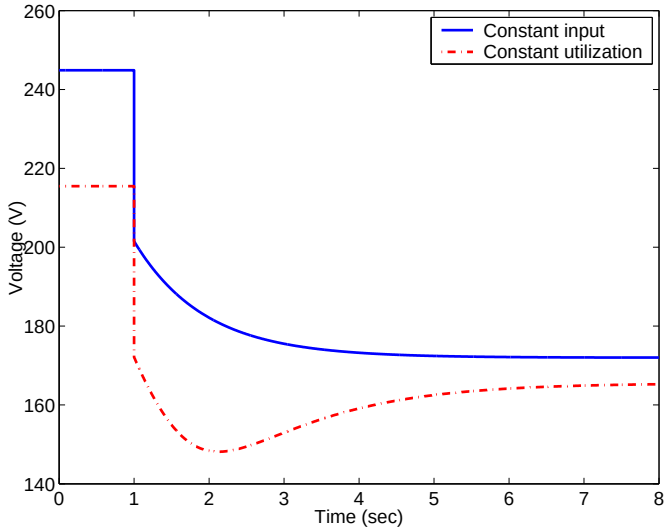

Fig. 3. SOFC voltage response to a current step.

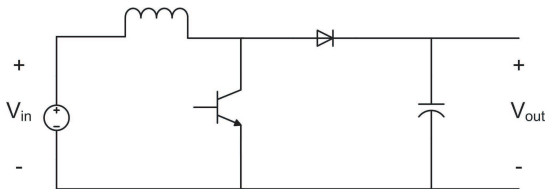

Fig. 4. Boost converter circuit diagram.

Figure 3 shows the fuel cell voltage in response to a step change in current from 500 A to 750 A for the SOFC model operating in the two different modes. The initial jump in voltage in both cases is due to the change in the three voltage drops caused by the current step. The voltage then settles to its new steady-state value. The constant utilization curve exhibits a second-order response due to the effect of the fuel processor dynamics, while the constant input case does not. Similar findings are reported in [4].

III. GRID INTERFACE

A. DC-DC converter and controls

A dc-dc converter is used to step up the voltage of the fuel cell stack to that of the dc bus, and to provide regulation of the DC bus voltage and of the fuel cell current [12]. The circuit diagram of a boost converter is shown in Figure 4 [13]. The model in this paper is not concerned with the switching dynamics of the converter. Accordingly, the inductor dynamics are not modeled. It is assumed that an ultra-capacitor is used for energy storage on the DC bus. Since a differential equation must be included for this device, its value of capacitance can include that of the converter capacitor. The topology of the DC bus model is shown in Figure 5.

Adopting an averaged model for the boost converter, the

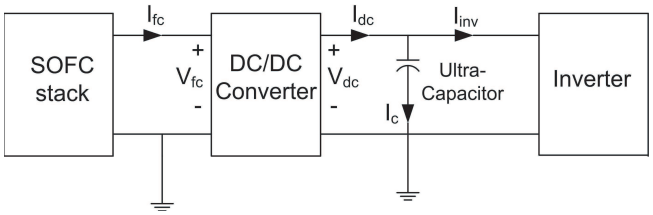

Fig. 5. DC bus topology.

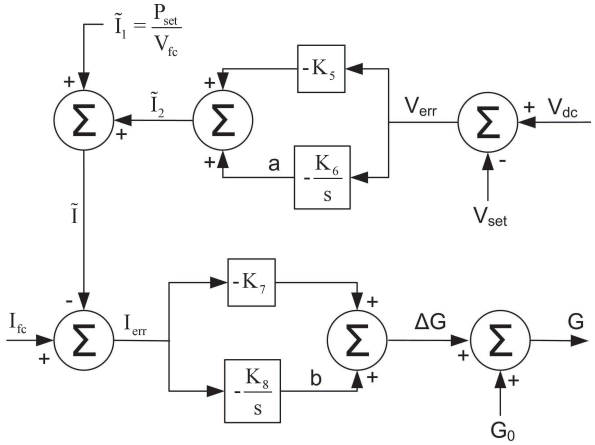

Fig. 6. DC-DC converter control scheme.

corresponding equations are as follows:

$$V_{dc} = GV_{fc} \tag{25}$$

$$I_{dc} = \frac{I_{fc}}{G} \tag{26}$$

$$I_{dc} = I_c + I_{inv} \tag{27}$$

where G is the gain of the converter. Capacitor dynamics are governed by the equation

$$\frac{d}{dt}\left(V_{dc}\right) = \frac{I_c}{C}, \tag{28}$$

where C is the capacitance.

The control scheme presented in this paper for the DC-DC converter employs two control loops. The block diagram for this system is shown in Figure 6. The inner loop regulates the DC bus voltage to a setpoint value by feeding the voltage error through a PI controller; this strategy is also proposed in [12]. The outer loop regulates the fuel cell current to a value corresponding to the power setpoint for the SOFC plant, which is fed from the inverter control system (described later). Specifically, the current setpoint is the ratio of the power setpoint to the fuel cell voltage. The output from the voltage controller is then added to this setpoint current. The current error is fed through a PI controller, the output of which is added to the nominal gain of the converter to produce the new value of converter gain. The corresponding model equations are as follows:

$$\tilde{I}_1 = \frac{P_{set}}{V_{fc}} \tag{29}$$

$$V_{err} = V_{dc} - V_{dc}^{set} \tag{30}$$

$$\frac{d}{dt}\left(a\right) = -K_6 V_{err} \tag{31}$$

$$\tilde{I}_2 = a - K_5 V_{err} \tag{32}$$

$$\tilde{I} = \tilde{I}_1 + \tilde{I}_2 \tag{33}$$

$$I_{err} = I_{fc} - \tilde{I} \tag{34}$$

$$\frac{d}{dt}\left(b\right) = -K_8 I_{err} \tag{35}$$

$$\Delta G = b - K_7 I_{err} \tag{36}$$

$$G = G_0 + \Delta G. \tag{37}$$

B. Inverter model and controls

1) Inverter-grid interface model: The SOFC plant interfaces to the AC system through an inverter. A model for the inverter-grid interface is given in Figure 7. It consists of an "internal" bus at which the voltage-source inverter synthesizes an AC voltage waveform, and the "terminal" bus that is common with the grid. The corresponding voltage phasors are $V_i\angle\delta_i$ and $V_t\angle\delta_t$, respectively, where the phase angles are specified with respect to a global reference sinusoid of nominal frequency. These two buses are connected through a transformer, with impedance jX. All quantities are expressed in per-unit.

The inverter seeks to regulate the active power P_{gen} delivered to the grid, and the terminal bus voltage magnitude V_t. This is achieved by controlling the modulation index m of the inverter as well as the inverter firing angle, which is equivalent to the phase δ_i of the synthesized voltage waveform. A similar control strategy is proposed in [14]. It is important to keep in mind that the inverter has no knowledge of the global reference. Accordingly, the absolute phase angle δ_i is meaningless. Rather, the phase of the inverter voltage must be established relative to a local reference signal. A phase-locked loop (PLL) is often used to provide that local reference.

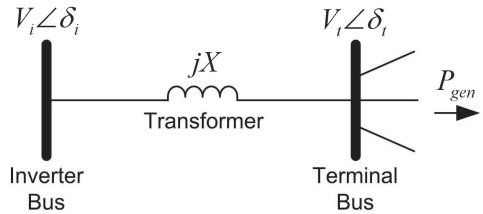

Fig. 7. Inverter-grid interface.

2) Phase-locked loop: Synchronizing the inverter and grid AC voltage waveforms can be achieved using a phase-locked loop (PLL). A block diagram displaying the functional components of a PLL is given in Figure 8. The measured sinusoid is mixed with the cosine generated by the PLL oscillator. This mixing process effectively establishes the phase difference between the two waveforms. That error signal is filtered and fed back to the voltage-controlled oscillator. The outcome is

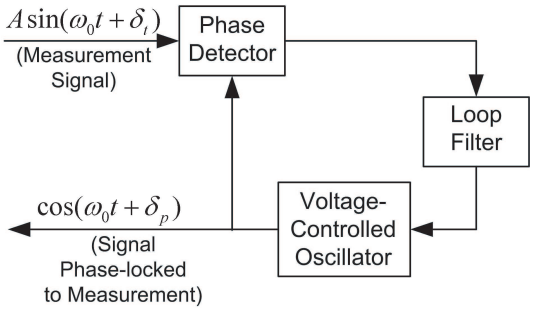

Fig. 8. Generic PLL block diagram.

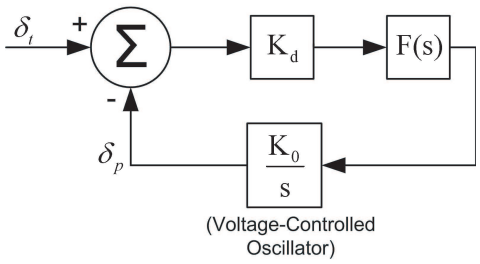

Fig. 9. Linearized PLL block diagram.

a signal that is phase locked to the measurement. Standard simplifying assumptions [15] allow the PLL to be modelled according to the linear block diagram of Figure 9. This model is commonly used for analysis and design of PLL-based systems [15]. Note though that the PLL has no knowledge of the global synchronous reference, and hence cannot determine the absolute angles δ_t and δ_p. The phase difference $\delta_t - \delta_p$ is, however, available locally.

Relating back to the inverter-grid connection of Figure 7, the PLL input is given by the terminal bus voltage $v_t(t)$, which has phase angle δ_t relative to the global reference sinusoid. If the grid frequency experiences a constant offset from nominal, then δ_t will by time-varying. To achieve zero offset between δ_t and δ_p under such circumstances, the PLL transfer function $F(s)$ should take the form

$$F(s) = \frac{K}{s}.$$

From Figure 9, this gives $\delta_p = \frac{K_d K K_o}{s^2}(\delta_t - \delta_p)$. Rewriting as a differential equation, with $K_3 = K_d K K_o$, and defining

$$\dot{\delta}_p = \omega_p \tag{38}$$

gives

$$\dot{\omega}_p = K_3(\delta_t - \delta_p). \tag{39}$$

An estimate of the deviation of system frequency from nominal is provided by ω_p. This can be used in the droop characteristic of the inverter controls.

3) Inverter control: As mentioned previously, the control objectives are to regulate the terminal bus voltage magnitude V_t, and the active power delivered to the grid P_{gen}. The first objective can be achieved by simple integral control

$$\dot{m} = K_1(V_{set} - V_t) \tag{40}$$

where V_{set} may be constant, or may follow a droop characteristic that is dependent upon the reactive power delivered to the grid. The inverter internal bus voltage is then given by

$$V_i = \frac{mV_{dc}}{V_{base}} \tag{41}$$

where V_{base} is the per-unit base voltage for the DC bus and inverter. From Figure 7, the active power delivered to the grid is given by

$$P_{gen} = \frac{V_i V_t}{X}\sin(\delta_i - \delta_t). \tag{42}$$

This quantity must also be equal to the power on the DC side of the inverter after making the per-unit conversion,

$$P_{gen} = \frac{V_{dc} I_{inv}}{P_{base}}. \tag{43}$$

Assuming V_i and V_t remain relatively constant, regulation of P_{gen} can be achieved by controlling the angle difference $\delta_i - \delta_t$. The PLL output δ_p provides a filtered version of δ_t though, so it is preferable to control

$$\theta = \delta_i - \delta_p. \tag{44}$$

Integral control gives,

$$\dot{\theta} = K_2(P_{set} - P_{gen}). \tag{45}$$

The active power setpoint P_{set} is determined from the droop characteristic

$$P_{set} = P^0 - R\omega_p, \tag{46}$$

where ω_p is the estimated frequency deviation provided by the PLL, see (38), and R is the droop constant.

The following analysis shows, however, that interactions between this P_{gen} controller and the PLL dynamics cause sustained oscillations. Rearranging (44) and substituting into (39) gives

$$\dot{\omega}_p = K_3(\delta_t - \delta_i + \theta). \tag{47}$$

Referring to (42), if P_{gen}, V_i and V_t are constant, then $\delta_i - \delta_t$ must also be constant. Under those conditions, differentiating (47) and substituting (45) and (46) gives

$$\begin{aligned}\ddot{\omega}_p &= K_3\dot{\theta} \\ &= K_2K_3(P^0 - R\omega_p - P_{gen})\end{aligned}$$

which implies

$$\ddot{\omega}_p + K_2K_3R\omega_p = K_2K_3(P^0 - P_{gen}). \tag{48}$$

This second order system is undamped. Any disturbance will lead to unattenuated oscillations in ω_p, even when P_{gen}, V_i and V_t are all constant.

Viable control requires the addition of a damping term to (48). This can be achieved by adding an extra term into (39),

$$\dot{\omega}_p = K_3(\delta_t - \delta_p) + K_4\dot{\theta}. \tag{49}$$

Differentiating, as above, and making similar substitutions results in

$$\begin{aligned}\ddot{\omega}_p &= K_3\dot{\theta} + K_4\ddot{\theta} \\ &= K_2K_3(P^0 - R\omega_p - P_{gen}) + K_2K_4(-R\dot{\omega}_p)\end{aligned}$$

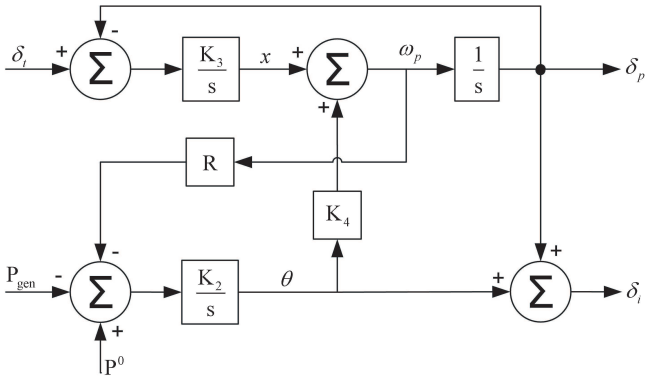

Fig. 10. PLL and active power regulation block diagram.

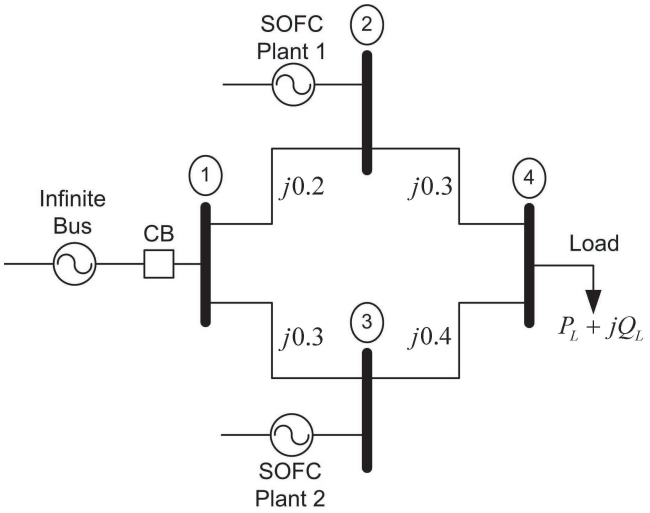

Fig. 11. Example power system.

and hence

$$\ddot{\omega}_p + K_2K_4R\dot{\omega}_p + K_2K_3R\omega_p = K_2K_3(P^0 - P_{gen}). \quad (50)$$

Further rearranging gives

$$\frac{1}{K_2}\ddot{\omega}_p + K_4R\dot{\omega}_p + K_3R\omega_p = K_3(P^0 - P_{gen}) \quad (51)$$

which reveals that $1/K_2$ acts like an inertia constant, and damping is provided by K_4R.

Defining the algebraic relationship

$$x = \omega_p - K_4\theta \quad (52)$$

allows (49) to be rewritten

$$\dot{x} = K_3(\delta_t - \delta_p). \quad (53)$$

Bringing the complete control strategy together gives,

$$\begin{aligned}
\dot{m} &= K_1(V_{set} - V_t)\\
\dot{\theta} &= K_2(P_{set} - P_{gen})\\
\dot{x} &= K_3(\delta_t - \delta_p)\\
\dot{\delta}_p &= \omega_p\\
0 &= V_i - \frac{mV_{dc}}{V_{base}}\\
0 &= P_{set} - (P^0 - R\omega_p)\\
0 &= \theta - (\delta_i - \delta_p)\\
0 &= x - (\omega_p - K_4\theta)\\
0 &= P_{gen} - \frac{V_{dc}I_{inv}}{P_{base}}.
\end{aligned}$$

The PLL and power regulator are described by the block diagram of Figure 10.

IV. Microgrid Simulations

The microgrid shown in Figure 11 will be used to illustrate the dynamic behaviour of the model components. SOFC plants are located at buses 2 and 3, and a constant power load is connected to bus 4. Bus 1 forms the interface between the microgrid and the rest of the power system, which is modelled as an infinite bus.

All of the AC quantities are expressed as per-unit values. A power base of 100 kVA is used in connecting the SOFC plant models to the inverter and grid models. A voltage base of 240 V was chosen for the DC buses and inverters. Since the DC bus setpoint voltage is 480 V, this causes the nominal value of the modulation index to be 0.5. The actual voltage of the grid is irrelevant.

For this example, the SOFC stacks are running in constant utilization mode with the parameters given in Table I, and a hydrogen utilization setpoint $\tilde{U}_{H_2} = 0.8$. The inverters and DC bus components have the parameters given in Table II. Plant 1 has a power setpoint of 0.7 pu (70 kW), and Plant 2 has a power setpoint of 0.6 pu (60 kW). The active and reactive power of the load, P_L and Q_L, are 1.7 pu and 0.6 pu, respectively, and the voltage of the infinite bus is set to 1 pu. The circuit breaker (CB) connecting bus 1 to the rest of the grid is initially closed. The two fuel cell plants together supply 1.3 pu of the active power demanded by the load. The remaining 0.4 pu active power is drawn from the main grid through bus 1. At 1 s, the CB opens. The constant load must now be supplied by the fuel cell plants. At 7 s, the CB is signaled to close, but closing is prevented until the voltage magnitude appearing across the CB contacts reduces to a given threshold. For this simulation, the threshold is set to $\sqrt{0.05}$ pu.[2] Consequently, the CB actually closes at 13.01 s.

Figure 12 shows the power generated by each of the SOFC plants over the simulation period, and Figure 13 shows the frequency deviation given by the inverter PLLs. When the microgrid is initially disconnected from the main grid, the powers generated by the SOFC plants immediately increase to compensate for the lost grid supply. Microgrid frequency drops in accordance with the droop characteristic. Note that Plant 1, which has a higher power setpoint, overshoots when the CB opens, while Plant 2 does not. The sum of the two power outputs must always equal the active power of the load while the CB is open. When the CB closes again, the phase relationship between the inverter voltages and the grid is such that active power initially flows from the microgrid to the infinite bus. Therefore, both plants see a power spike

[2]For numerical reasons, the simulation actually monitors the square of the voltage magnitude.

TABLE II

SOFC-INVERTER PLANT PARAMETERS.

parameter	value
K_1	10
K_2	20
K_3	20
K_4	10
D	0.4
X	0.2pu
V_{set}	1pu
K_5	5
K_6	25
K_7	10
K_8	25
C	0.1F
V_{dc}^{set}	480V

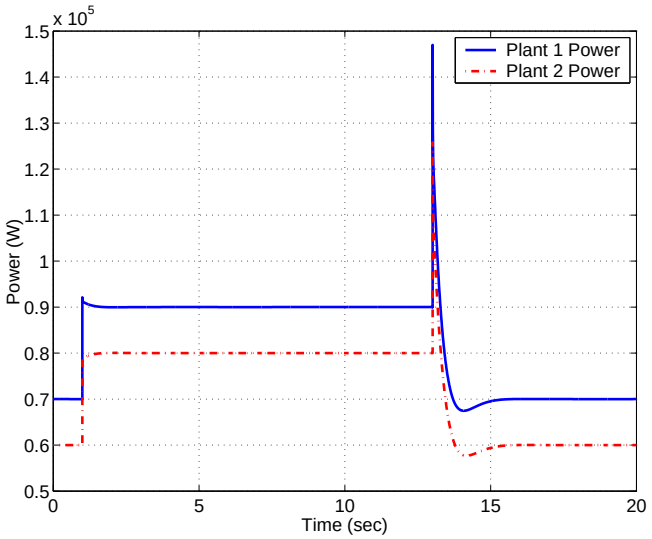

Fig. 12. Power output of SOFC plants.

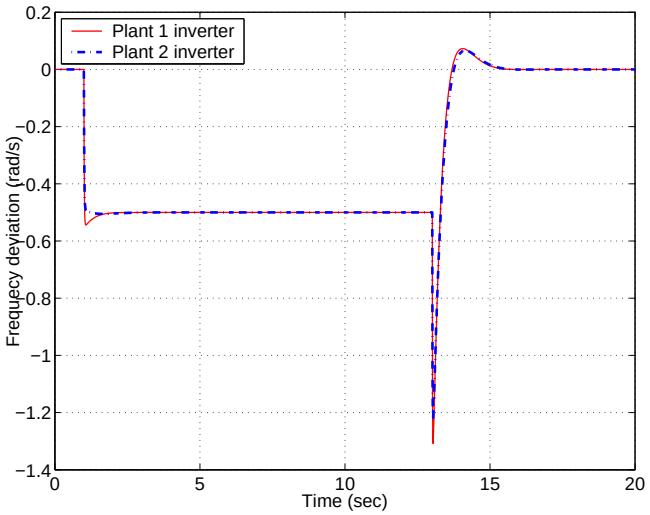

Fig. 13. PLL frequency deviation of inverters.

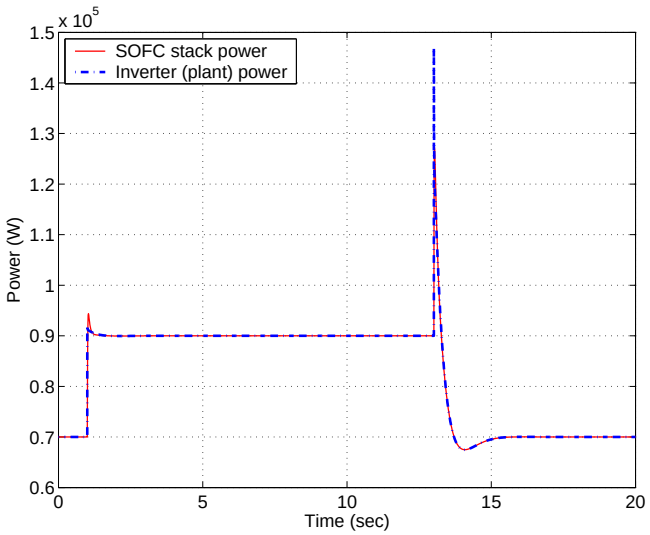

Fig. 14. SOFC stack and plant power for Plant 1.

immediately following the reconnection. The inverter controls respond accordingly, with active power outputs quickly returned to their pre-disturbance values, and microgrid frequency restored to the nominal value.

Figure 14 shows the power output of the SOFC stack for Plant 1 as well as the inverter output. When the power output makes a sudden increase, the inverter is able to provide more power than the fuel cell stack alone due to the presence of the capacitor on the DC bus. As the transients subside, the stack power overshoots the inverter power at times, allowing the capacitor to recharge.

Figure 15 shows the variation of the DC bus voltage of Plant 1 during the simulation period. Each time the power output increases, the voltage makes a sudden drop due to the discharging of the capacitor, but the DC-DC converter controls then restore it to the setpoint value.

Figure 16 shows angle behaviour during the disturbance. (Only Plant 1 inverter quantities are shown.) When the CB opens, the inverter terminal bus voltage undergoes an immediate phase shift. Over the subsequent period of autonomous operation, the microgrid frequency is below nominal. Accordingly, the microgrid phase angle, relative to a global reference at nominal frequency, displays a steady decrease. This continues until the CB closes. At that instant, the microgrid voltages are out of phase with the stronger system. In response, the inverter terminal bus phase angle adjusts very rapidly, quickly settling to a value that is exactly 2π rad behind its initial value.

Figure 16 also shows that the PLL angle closely tracks the terminal bus angle. The difference between these quantities is shown more clearly in Figure 17. It can be seen that the controller is effective in rapidly driving this difference to zero. The angle difference across the inverter transformer is also shown in Figure 17. Notice that when the CB closes, the resulting phase shift in the inverter terminal bus voltage causes a spike in the angle difference across the inverter transformer. That spike in angle difference underlies the spike in active power P_{gen} observed in Figure 12.

V. CONCLUSIONS

A model for an SOFC stack, operating at relatively low pressures, has been developed. The model incorporates the

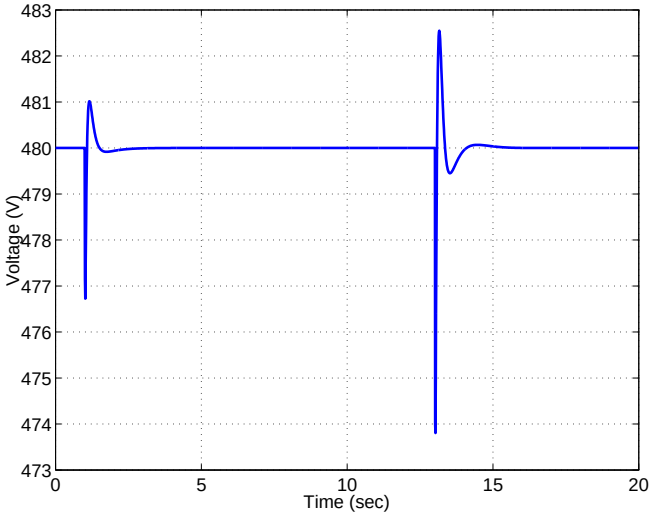

Fig. 15. DC bus voltage for Plant 1.

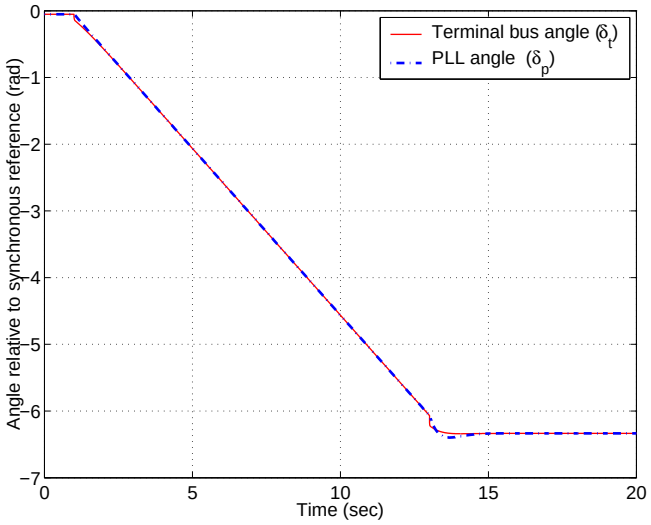

Fig. 16. Plant 1 inverter angle behaviour relative to a global reference.

electrochemical reaction dynamics and the major voltage losses in SOFCs, but is not concerned with the thermal dynamics. It uses average partial pressure ideas, consistent with [3], [6], but differs in the modeling of the anode and cathode outflows. In particular, unchoked flow is assumed.

The two basic modes of operation of fuel cells are constant input and constant utilization. In the former, the flow rate of fuel (hydrogen) into the anode channel is constant, whereas in the latter, it is controlled so as to regulate the ratio of fuel used to fuel supplied. In the latter mode, a step change in SOFC stack current causes a second-order response in the stack voltage. This is due to the dynamics of the fuel processor, which limits the rate at which the hydrogen input flow rate can change.

A DC-DC boost converter is used to raise the voltage of the SOFC stack to that of the DC bus, where an ultra-capacitor provides energy storage. The proposed control system for the boost converter consists of two loops. The inner loop regulates the DC bus voltage, while the outer loop regulates the fuel

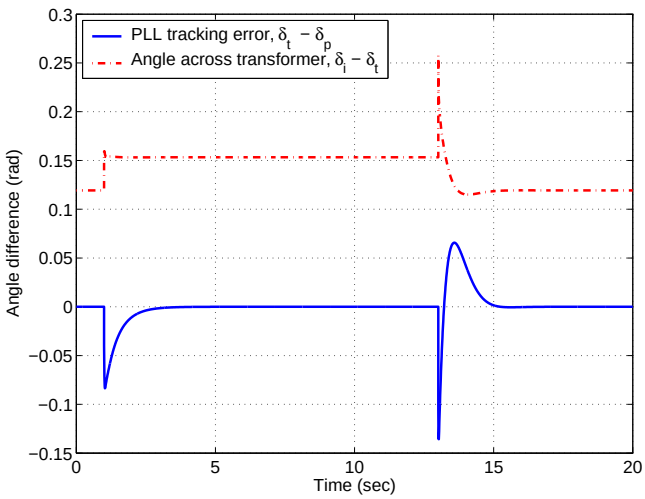

Fig. 17. Plant 1 inverter angle differences.

cell current to a value consistent with the plant's active power setpoint.

An inverter interfaces the SOFC plant to the AC grid. The proposed control strategy adjusts the modulation index of the inverter to regulate the grid-side voltage magnitude, and adjusts the firing angle of the inverter to regulate the active power delivered to the grid. The latter utilizes a phase-locked loop (PLL) to provide a local phase angle reference for the inverter, since the phase with respect to a global reference is not available to the plant. The PLL introduces additional dynamics to the system.

An example system, in which two SOFC plants provide power to a microgrid, has been presented. In the example, the microgrid was initially connected to the main grid, and was subsequently disconnected. During autonomous operation, the microgrid operated at a frequency below nominal due to droop control. At reconnection, microgrid voltages were out of phase with the stronger system. This resulted in a step in the phase angle difference across the transformers connecting the inverters to the grid, causing a spike in their power outputs. Inverter controls quickly responded, returning the power outputs to their setpoint values, and the microgrid frequency to nominal. During power output spikes, the inverters were able to provide more power than the stacks alone because of the energy stored in the DC bus capacitors. The DC-DC converter controls allowed the capacitors to subsequently recharge, while driving the DC bus voltages back to their setpoint values.

REFERENCES

[1] C. Smallwood, "Distributed generation in autonomous and non-autonomous micro grids," in *Proceedings of the IEEE Rural Electric Power Conference*, Colorado Springs, CO, May 2002, pp. D1.1–D1.6.

[2] F. Katiraei and M. Iravani, "Power management strategies for a microgrid with multiple distributed generation units," *IEEE Transactinos on Power Systems*, vol. 21, no. 4, pp. 1821–1831, May 2006.

[3] J. Padulles, G. W. Ault, and J. R. McDonald, "An integrated SOFC plant dynamic model for power systems simulation," *Journal of Power Sources*, vol. 86, pp. 495–500, 2000.

[4] C. Wang and M. H. Nehrir, "A physically-based dynamic model for solid oxide fuel cells," *IEEE Transactions on Energy Conversion*, to appear.

[5] R. O'Hayre, S.-W. Cha, W. Colella, and F. B. Prinz, *Fuel Cell Fundamentals*. New York, NY, USA: John Wiley & Sons, Inc., 2006.
[6] K. Sedghisigarchi and A. Feliachi, "Dynamic and transient analysis of power distribution systems with fuel cells - Part I: fuel-cell dynamic model," *IEEE Transactions on Energy Conversion*, vol. 19, no. 2, pp. 423–428, June 2004.
[7] J. Larminie and A. Dicks, *Fuel Cell Systems Explained*, 2nd ed. Chinchester, England, UK: John Wiley and Sons, Ltd., 2003.
[8] J. F. Blackburn, G. Reethof, and J. Shearer, Eds., *Fluid Power Control*. Cambridge, MA, USA: The Technology Press of M.I.T. and John Wiley & Sons, Inc., 1960, pp. 214–219.
[9] E. fundamentals, "Orifice flowmeter calculator," Website (http://www.efunda.com/formulae/fluids/calc_orifice_flowmeter.cfm), Apr. 2006.
[10] E. N. Viall and Q. Zhang, "Determining the discharge coefficient of a spool valve," in *Proceedings of the American Control Conference*, vol. 5, June 2000, pp. 3600–3604.
[11] Y. Zhu, "Analysis and control of distributed energy resources," Ph.D. dissertation, Washington State University, May 2002.
[12] C. Wang and M. H. Nehrir, "Short-time overloading capability and distributed generation applications of solid oxide fuel cells," *IEEE Transactions on Energy Conversion*, to appear.
[13] P. T. Krein, *Elements of Power Electronics*. Oxford University Press, 1998.
[14] K. Sedghisigarchi and A. Feliachi, "Dynamic and transient analysis of power distribution systems with fuel cells - Part II: control and stablility enhancement," *IEEE Transactions on Energy Conversion*, vol. 19, no. 2, pp. 429–434, June 2004.
[15] D. Abramovitch, "Phase-locked loops: a control centric tutorial," in *Proceedings of the American Control Conference*, Anchorage, AK, May 2002.